Fuel Surrogate Physical Property Effects on Direct Injection Spray and Ignition Behavior

Doohyun Kim, Jason Martz, Angela Violi

University of Michigan, Department of Mechanical Engineering, Ann Arbor, MI 48109

Corresponding author: Angela Violi (avioli@umich.edu)
1301 Beal Ave. Ann Arbor, MI 48109
(734) 615 - 6448

Keywords: Fuel properties, liquid penetration, ignition delay, spray simulation, CFD, surrogate

Report Documentation Page

Form Approved
OMB No. 0704-0188

1. REPORT DATE	2. REPORT TYPE	3. DATES COVERED
01 SEP 2015		**00-00-2015 to 00-00-2015**

4. TITLE AND SUBTITLE	5a. CONTRACT NUMBER
Fuel Surrogate Physical Property Effects on Direct Injection Spray and Ignition Behavior	5b. GRANT NUMBER
	5c. PROGRAM ELEMENT NUMBER
6. AUTHOR(S)	5d. PROJECT NUMBER
Doohyun Kim; Jason Martz; Angela Violi	5e. TASK NUMBER
	5f. WORK UNIT NUMBER
7. PERFORMING ORGANIZATION NAME(S) AND ADDRESS(ES)	8. PERFORMING ORGANIZATION REPORT NUMBER
US Army RDECOM-TARDEC,6501 E. 11 Mile Road,Warren,MI,48397-5000	
9. SPONSORING/MONITORING AGENCY NAME(S) AND ADDRESS(ES)	10. SPONSOR/MONITOR'S ACRONYM(S)
	11. SPONSOR/MONITOR'S REPORT NUMBER(S)

12. DISTRIBUTION/AVAILABILITY STATEMENT
Approved for public release; distribution unlimited

13. SUPPLEMENTARY NOTES

14. ABSTRACT
See Report

15. SUBJECT TERMS

16. SECURITY CLASSIFICATION OF:			17. LIMITATION OF ABSTRACT	18. NUMBER OF PAGES	19a. NAME OF RESPONSIBLE PERSON
a. REPORT	b. ABSTRACT	c. THIS PAGE			
unclassified	**unclassified**	**unclassified**	**Same as Report (SAR)**	**34**	

1 Introduction

Typical hydrocarbon fuels used in internal combustion engines, such as gasoline, diesel, or jet fuel, are composed of hundreds to thousands of hydrocarbon (HC) species. Such a large number of species in high fidelity Computational Fluid Dynamics (CFD) with detailed chemistry is beyond our current computational capability. Therefore, surrogate fuels and their associated chemical mechanisms have been developed and utilized to represent the combustion behavior of typical HC fuels within CFD simulations. The most common surrogate formulation approach seeks to match the combustion related properties of the target fuel [1–5]. This approach requires reliable models of the HC mixture properties for mathematical optimization, which determines the surrogate composition that minimizes the deviation from the target properties. For modern diesel engines, which employ direct fuel injection, the physical properties of liquid fuel influence the spray, mixture development and ultimately the ignition and combustion process [6]. To more accurately predict the diesel combustion process, it is very important to understand which fuel properties have a major impact on the combustion physics within the targeted device in order to emphasize those properties in future surrogate formulations.

To date, most studies into the importance of liquid fuel physical properties to combustion behavior have been experimental. Experimental studies by Naber and Siebers [7] and Siebers [8,9] investigated the effect of various parameters on liquid penetration under diesel relevant conditions and observed that lower fuel volatility results in longer liquid length. Higgins et al. [10] tested nine different fuels and proposed a liquid penetration correlation as a function of fuel density and the energy required to vaporize the liquid fuel. Genzale et al. [11] compared diesel and biodiesel sprays under conditions relevant to late-cycle post-injection conditions and showed ~15 % longer liquid penetration length for biodiesel. Kook and Pickett [12] tested various types of jet fuels and showed that while liquid penetration length is affected by liquid density and volatility, the variations in vapor penetration length for different fuels were within the experimental uncertainties. Wu et al. [13] observed that the viscosity of oxygenated fuels

influences spray atomization behavior. Other experimental comparisons have been made to assess the sensitivity of engine performance, emissions, and spray characteristics to the properties of alternative diesel fuels, such as dimethyl ether (DME), biodiesel, and jet fuel, which are significantly different from those of petroleum derived diesel fuel [14–18].

While these experiments provided valuable insights, it is difficult to isolate the effect of each property by simply comparing results from different fuels. Computational studies offer a more effective approach to isolate physical fuel property effects from the complex processes occurring during spray combustion. Only a limited number of numerical investigations have examined liquid fuel property effects, including Som et al. [19], who quantified the differences between the injection and spray characteristics of biodiesel and diesel fuel. Pei et al. [20] conducted a sensitivity analysis with a diesel engine simulation to assess the relative effects of various physical properties including density, heat of vaporization, vapor pressure, and viscosity. While parameters other than fuel properties (such as select model constants and injector-related parameters) were shown to be the most sensitive variables, the liquid fuel density was shown to affect ignition delay, combustion phasing, and emissions. The CFD simulations by Ra et al. [21] showed that of all of the physical properties considered in their study, density, vapor pressure, and surface tension were predicted to have the most influence on cylinder pressure and combustion phasing. However, this study focused on the sensitivity of engine performance parameters rather than how the physical property variations affect the spray formation and ignition behavior.

The focus of the current work is on the effect of temperature-dependent physical properties of the liquid fuel (such as density and viscosity) on spray penetration, the evolution of the local thermodynamic states within the jet, and the ignition delay period of compression ignited combustion. These effects are predicted with a validated CFD simulation of a free fuel jet. Through such efforts, the surrogate optimization processes can be better informed by understanding which fuel physical properties have the largest impact on the diesel ignition

process and the relative importance of these properties for the development of future fuel surrogates.

2 Methodology

2.1 Spray modeling set up

Spray characteristics were predicted under diesel-relevant conditions with the CFD package CONVERGE [22]. The two-phase processes within the spray were modeled with the Lagrangian-Droplet and Eulerian-Fluid approach. The Reynolds Averaged Navier Stokes (RANS) equations with the RNG k-ε model were utilized to model the turbulence in the gas-phase flow field. Automatic mesh refinement and fixed embedding near the nozzle were used to increase the spatial resolution of the solution with a minimum increase in computational expense [22].

The dynamics of the fuel spray droplet were described with a number of phenomenological and physical models. The blob injection method of Reitz and Diwakar [23] was employed. The Kelvin-Helmholtz – Rayleigh-Taylor (KH-RT) model without the use of an ad hoc breakup length definition was used to predict the breakup and atomization of the injected fuel parcels [22]. Liquid droplet collision and coalescence was modeled with the No Time Counter collision model [24] in conjunction with the Post collision outcome model [25]. The dynamic drop drag model of Liu et al. [26] was utilized to account for the change of the drag coefficient due to droplet deformation. A standard droplet turbulent dispersion model [27] was included, while droplet evaporation was predicted with the Frossling correlation [27]. Based on the work of Senecal et al. [28] which showed the asymptotic convergence of the spray characteristics with grid refinement, the minimum grid size in the adaptive mesh refinement algorithm and the total number of injected parcels were set to 0.25 mm and 512,000, respectively; the base mesh size was 2 mm.

Pure n-dodecane, which is often used as an n-alkane representative for jet fuel and diesel surrogates [29,30], was used as the fuel in the current work. Temperature-dependent physical properties of liquid n-dodecane were taken from the DIPPR database [31]. A recently published reduced mechanism with 255 species and 2289 reactions was used to model the oxidation of n-dodecane [32]. The mechanism has been validated against several experimental data sets, including ignition delay times from shock tube and rapid compression machine studies, species time histories obtained from shock tube experiments, concentration profiles from a pressurized flow reactor, and laminar flame speed. Specifically, the ignition delay times calculated with the mechanism were shown to follow experimental measurements over a wide range of temperatures (750 K ~ 1400 K), pressures (12 atm ~ 46 atm) and equivalence ratios ($\Phi = 0.5 \sim 1$).

2.2 Model validation

The model was validated by comparison with experimental data from a constant-volume combustion chamber at Sandia National Laboratories [33–35] that utilized the Spray A injector (serial number 210677). Liquid/vapor penetration lengths and vaporized fuel mass fraction distributions from two non-reacting spray experiments (900 K, 6 MPa and 1100 K, 5 MPa) were used, along with ignition location and ignition delay times from three reacting spray experiments(750 K, 5 MPa, 900 K, 6 MPa, and 1200 K, 8 MPa). The ambient temperatures and pressures of validation cases are relevant to the conditions in diesel engines. More details of the n-dodecane spray experiments are summarized in Table 1. The injector specifications, the rate of injection profile and all of the boundary conditions for the simulations were taken from the experiments. In the CFD simulations, the liquid penetration length was defined as the axial distance from the nozzle exit to the region that encompasses the 95th percentile of the total liquid fuel mass at a given time, while the vapor penetration length was defined as the maximum axial distance from the nozzle exit to where the fuel mass fraction is 0.1 %. The ignition delay in the

simulations was defined as the time after the start of the injection when maximum rise rate of peak temperature occurs.

Figure 1 shows good agreement between the predicted and experimental liquid and vapor penetration lengths as a function of time for non-reacting spray simulations. The uncertainties associated with the experimental measurements were less than 1 mm for most of the data points [33]. While improvements are needed for predicting the initial transients of the liquid penetration, the model is able to predict stabilized liquid penetration lengths and the overall trend of vapor penetration. The root mean squared errors of the stabilized liquid penetration and vapor penetration lengths were 0.4 mm and 2.8 mm for the 900 K 22.8 kg/m^3 case, and 0.8 mm and 2.9 mm for the 1100 K 15.2 kg/m^3 case.

The steady-state radial and axial distributions of the vapor fuel mass fraction are compared in Figure 2. The simulation results were taken at 1.4 ms after the start of injection, when the jet was steady. As shown in Figure 2, the model was capable of capturing the general radial and axial fuel vapor distribution trends. At 25 mm downstream from the injector tip, the predicted radial mass fractions for the two test cases were largely within the experimental uncertainties. For the axial distribution at the jet centerline, the fuel vapor mass fraction for 900 K, 22.8 kg/m^3 was within the experimental uncertainties from ~20 mm to ~30 mm however the fuel vapor mass fraction was under-predicted for larger axial distances. The calculated axial vapor fuel fraction was in better agreement with experiments for the 1100 K, 15.2 kg/m^3 case.

For the reacting spray simulations, the n-dodecane reaction mechanism [32] was included without changing any of the spray model parameters used in non-reacting set up. All of the ambient conditions were taken from experiments, with the exception of the ambient temperature of 750 K 22.8 kg/m^3 case, which needed to be increased by 30 K for reasonable agreement with experimental ignition delay time. Figure 3 shows ignition delays from the simulation and experiments. Although ignition delay times are slightly over-predicted, the model is shown to be capable of capturing the ignition delay trend over a wide range of temperature. Figure 4 compares high temperature chemiluminescence images from the experiments versus the local

temperatures from the simulation near the time of ignition to validate the spatial ignition location. As seen for all three cases, the model is capable of qualitatively predicting the spatial locations of high temperature chemiluminescence with the highest temperature regions near the start of the ignition.

The above comparisons show that the model successfully captures the experimental liquid and vapor penetration lengths, the spatial fuel vapor distribution at steady state for non-reacting spray, along with ignition delay time and ignition location for reacting spray. This modeling set up was used as the baseline for the following simulations where physical properties are perturbed.

2.3 Liquid physical property perturbation

A sensitivity analysis was conducted with reacting spray simulations at two ambient conditions (900 K 22.8 kg/m^3, and 750 K 22.8 kg/m^3) to identify the liquid fuel properties that are of significance to the liquid spray penetration length and ignition delay. Six liquid physical properties that appear in the spray models of the current work were examined here, including density, vapor pressure, viscosity, surface tension, heat of vaporization, and specific heat capacity. Beginning with the baseline n-dodecane properties, the individual fuel properties were perturbed one at a time by multipliers which were determined to cover the minimum and maximum property values of the various types of hydrocarbons used in recent surrogate studies [1–3]. N-heptane, n-decane, iso-octane and iso-cetane were considered for linear alkanes; methylcyclohexane and decalin for cycloalkanes; toluene, 1,3,5-trimethylbenzene and n-propylbenzene for aromatics. The reason for implementing this method rather than a more conventional approach using consistent relative changes of each property was that the properties considered in this study have a drastically different range of property magnitudes among the various species. For example, decalin has the highest density among the above pure components, which is about 20 % greater than that of n-dodecane. However, n-heptane has highest vapor

pressure, which is 10 ~ 20 times greater than that of n-dodecane, depending on temperature. Due to this significant difference among the properties, perturbing the properties with a common multiplier does not represent the real property variations within the surrogate components. Therefore, multiplier perturbation was performed with this approach and summarized in Table 2.

The modeling parameters were maintained from the baseline case for all of the perturbation simulations, with the exception of the injected fuel mass flow rate for the density perturbation study. This change was necessary in order to maintain the baseline pressure drop across the injector orifice and the incoming jet momentum flow rate. The relationship among the mass flow rate, the pressure drop across orifice, the jet momentum flow rate, and liquid fuel density can be expressed using mass conservation and Bernoulli's equation as shown in [7,33].

$$\dot{m}_{fuel} = C_d \cdot A_{orifice} \cdot \sqrt{2 \cdot \left(P_{fuel} - P_{amb}\right) \cdot \rho_{fuel}} \qquad \text{(Eq. 1)}$$

$$\begin{aligned} \dot{M}_{fuel} &= \dot{m}_{fuel} \cdot U_f \\ &= 2 \cdot C_d \cdot C_v \cdot A_{orifice} \cdot \left(P_{fuel} - P_{amb}\right) \end{aligned} \qquad \text{(Eq. 2)}$$

where $\dot{m}_{fuel}$ is the fuel mass flow rate, C_d is the discharge coefficient, C_v is the velocity coefficient, $A_{orifice}$ is the orifice exit area, ρ_{fuel} is the liquid fuel density, U_f is the fuel velocity, P_{fuel} - P_{amb} is the pressure drop across the orifice and $\dot{M}_{fuel}$ is the momentum flow rate of the liquid fuel from the orifice. As seen in Equation 1, for a given pressure drop across the orifice, the fuel mass flow rate is proportional to the square root of the fuel density. Also, a constant pressure drop leads to constant jet momentum flow rate (Equation 2). This relationship has been experimentally validated by Genzale et al. [11] for sprays of regular diesel and higher density biodiesel at a constant injection pressure. Thus, for the density perturbation cases, all the parameters including the pressure drop across the orifice and jet momentum were maintained, while the injected fuel mass flow rate was proportional to the square root of density.

3 Results – liquid penetration length

Figure 5 summarizes the relative change in the liquid penetration length for the physical property perturbations. While perturbations of density, vapor pressure, viscosity, and specific heat resulted in ± 4 ~ 10 % changes in liquid penetration for the 900K case and ± 5 ~ 18 % changes for the 750 K case, surface tension and heat of vaporization perturbations showed only ± 2 % change in liquid penetration at most. Although all six physical properties considered in this study are included in one or more spray submodels (breakup model, evaporation model, etc.) as model parameters, this observation indicates that the impact of surface tension and heat of vaporization on the predicted liquid penetration length is considerably smaller than the other four properties under the conditions studied.

3.1 Viscosity and surface tension effects

It has been experimentally shown that greater liquid fuel viscosity and surface tension slow the droplet breakup and atomization process [36,37] which is a contributing factor to longer liquid penetration lengths. From a modeling standpoint, both viscosity and surface tension play the most significant role in spray breakup, as they determine the Reynolds and Weber numbers, which are key model parameters. It is apparent in Figure 5 that the simulations replicate the expected experimental trend – the liquid penetration length gets longer as viscosity and surface tension increase. However, the very small change in surface tension over the relatively large range of hydrocarbon molecules considered in this study does not have as significant effect on liquid penetration length. The more significant effect of viscosity in Figure 5 is consistent with previous experimental analysis [37], where viscosity, and not surface tension, was the dominating factor to changes in the Sauter Mean Diameter (SMD) of various liquid fuel sprays.

3.2 Specific heat and heat of vaporization effects

Another physical factor that influences liquid penetration length is the total thermal energy required to heat up and vaporize liquid fuel, as experimentally shown in Siebers [9] and Higgins et al. [10]. The correlation from these experiments implies that higher fuel specific heat and latent heat of vaporization results in longer liquid lengths. As a simple thermodynamic analysis, the instantaneous energy balance for a single liquid droplet with a uniform temperature that vaporizes when heated by the ambient can be used as follows.

$$A_d q_d = C_{p,liq} m_d \frac{dT_d}{dt} - \frac{dm_d}{dt} h_{vap} \qquad \text{(Eq. 3)}$$

where A_d is the droplet surface area, q_d is the heat flux from the ambient to the droplet, T_d is the droplet temperature, $C_{p,liq}$ is the specific heat of the fuel at T_d, m_d is the droplet mass at T_d, and h_{vap} is the heat of vaporization at T_d. Equation 3 implies that the heat transferred from the ambient to the liquid fuel is used either for increasing the liquid temperature or for causing the phase to change from liquid to vapor. When Equation 3 is integrated over the lifetime of the evaporating liquid droplet,

$$\int_{t_{init}}^{t_{end}} A_d q_d dt = \int_{T_{d,init}}^{T_{d,end}} C_{p,liq} m_d dT_d - \int_{m_{d,init}}^{m_d=0} h_{vap} dm_d$$

$$Q_{total} = \int_{T_{d,init}}^{T_{d,end}} \left(C_{p,liq} m_d - h_{vap} \frac{dm_d}{dT_d} \right) dT_d \qquad \text{(Eq. 4)}$$

where Q_{total} is the total thermal energy needed from the ambient to vaporize the liquid droplet, t_{init}, $T_{d,init}$ and $m_{d,init}$ are the initial time, temperature and mass of the droplet, and t_{end} $T_{d,end}$ is the final time and droplet temperature when the droplet mass reaches zero. Note $C_{p,liq}$, m_d, and h_{vap} are all functions of the droplet temperature. Since dm_d / dT_d is negative for a vaporizing droplet, it is clear from Equation 4 that higher specific heat and heat of vaporization will result in a greater amount of thermal energy required from the ambient to vaporize the liquid fuel. As seen in Figure 5, the simulation results are consistent with this analysis and the experimental

observations, where greater specific heat and heat of vaporization resulted in longer liquid penetration lengths.

However, contrary to the specific heat cases, the variation in the heat of vaporization causes only a very small change in liquid length. This is mainly due to the ambient pressures of the test conditions, which were much higher than the critical pressure of the liquid n-dodecane. Note that while the vapor pressure of n-dodecane increases exponentially until it reaches its critical pressure of 1.8 MPa at 658 K, the ambient pressures were ~6 MPa for the 900 K case and ~5 MPa for the 750 K case, which are relevant to the TDC conditions in compression ignition engines [9]. Under such high pressures, the conventional evaporation model used for the current study [27] predicts that the bulk of evaporation occurs at liquid temperatures close to the critical temperature where the vapor pressure is the highest, because the ratio between the vapor pressure of the liquid fuel and the ambient pressure is the key parameter driving evaporation. Figure 6 illustrates the fraction of evaporating mass within each liquid temperature bin (10 K) relative to the total evaporating mass at a given time step (0.2 ms) for the 900 K 22.8 kg/m^3 case, and clearly shows that the bulk of the phase change occurs at droplet temperatures over 600 K. $C_{p,liq}$ increases with liquid temperature, however h_{vap} decreases and eventually becomes zero at the critical temperature, as shown in Figure 7 for n-dodecane. Thus, with the liquid temperature approaching the critical temperature, the heat transfer needed for vaporization (Q_{total}) in Equation 4 is dominated by $C_{p,liq}$, with a much smaller contribution from h_{vap}. Therefore, in proximity to the critical temperature, the perturbation of the heat of vaporization has only a marginal effect on Q_{total}, which results in a much smaller change in liquid penetration relative to the specific heat perturbations.

3.3 Density effects

Liquid density has been shown to affect the liquid penetration length in spray experiments [7,10–12], and it is commonly reported that greater liquid fuel density resulted in

longer liquid penetration. The current simulation results in Figure 5 capture the expected trend, showing that the liquid penetration length is sensitive to liquid density variations. This effect is a result of the entrainment rate, which is defined as the ratio of entrained ambient mass to the fueling rate, which is inversely proportional to the square root of the fuel density as shown in [7,11,12]. Thus, a higher liquid density requires the entrainment of additional ambient air, which demands more mixing time or a greater mixing length to complete the vaporization process.

3.4 Vapor pressure effects

Vapor pressure, a measure of liquid volatility, is a well-known fuel property that affects liquid penetration [9,10,12] by influencing the vaporization process. Higher vapor pressure enhances liquid fuel vaporization, resulting in shorter liquid penetration, which is well captured by the current model in Figure 5. An interesting observation is that the effect of vapor pressure is much more significant in the lower temperature case. Figure 5 shows that the same perturbations in vapor pressure resulted in a 4 ~ 6 % relative change in the 900 K case, but in a 13 ~ 18 % change in the 750 K case. Because of much faster heat transfer to the liquid fuel for the higher ambient temperature case, the effect of fuel volatility on liquid penetration is less pronounced in the 900 K case.

4 Results - ignition delay time

To better understand the effect of fuel properties on the spray ignition characteristics under the tested conditions, the calculated global heat release rates for the baseline cases are shown in Figure 8 (a) for 900 K 22.8 kg/m^3 and (b) for 750 K 22.8 kg/m^3. Two-stage ignition is predicted for both cases, including low temperature heat release (LTHR), negative temperature coefficients (NTC) behavior, and high temperature ignition chemistry. The ignition timings shown in Figure 8 are defined as the time when the maximum rise rate of peak temperature occurs. The LTHR phase is defined as the period between the start of heat release and the first

heat release rate peak, while the NTC period is defined as the time from the first heat release rate peak to the start of ignition. The ignition process takes much longer for the 750 K case, primarily due to the longer duration of the LTHR and NTC phases.

Figure 9 shows the time evolution of the local temperatures during the ignition process for the 900 K 22.8 kg/m^3 case. In the temperature contour at 0.375 ms and 0.4 ms after the start of injection, the temperature rise due to LTHR is observed at the periphery of the spray where the equivalence ratio is 1~2. At 0.45 ms, high temperature chemistry is about to start in the interior of the spray where the fuel/air mixture is slightly rich and local temperature is the highest, which leads to the ignition of the fuel spray. A similar ignition process was predicted for the 750 K case (not shown), with the initial heat release at the periphery of the spray and the onset of high temperature heat release in the spray interior. Similar initial temperature rise at the periphery of the spray was also observed in Som and Aggarwal [38].

The location of initial heat release (0.375 ms and 0.4 ms in Figure 9) aligns well with regions of high local reactivity calculated using a methodology similar to the one shown in Kodavasal et al. [39]. In this case, the local reactivity is represented by the inverse ignition delay time calculated with the conditions of each cell in the fuel spray. The local temperature, pressure, and gas phase composition at a given instance are used to initialize the CHEMKIN homogeneous reactor code [40], which uses the same chemical mechanism as that in the CFD simulations to calculate the ignition delay time. A shorter ignition delay time is indicative of a more reactive mixture, hence the inverse of the calculated ignition delay time can be used to gauge local reactivity. Figure 10 illustrates the local reactivity distribution during LTHR for the 900 K 22.8 kg/m^3 case. It is seen that the most reactive charge is located at the periphery of the spray, where the temperature is higher than the interior and the equivalence ratio is near stoichiometric, which is in agreement with the location where initial temperature rise is observed. As time progresses, the highest temperature region shifts into the interior part of the spray as a result of heat and mass transfer.

Figure 11 summarizes the relative changes in ignition delay time with physical property perturbations for the (a) 900 K 22.8 kg/m^3 case and (b) 750 K 22.8 kg/m^3 case. For both conditions, the perturbations of specific heat and density have significant impact on the calculated ignition delay (-9.7 % ~ 9.1 % for specific heat, -7.1 % ~ 6.7 % for density); vapor pressure and the latent heat of vaporization have a small effect (-2.1 % ~ 0.7 %), while variations in viscosity and surface tension marginally affect ignition delay (less than 0.5 % at most). No meaningful deviations from the baseline cases could be observed for the viscosity and surface tension cases when local temperatures and equivalence ratio within the spray are compared, despite their effect on liquid length. On the other hand, the ignition delay time is sensitive to perturbations in specific heat and density, which are discussed in the following sections.

4.1 Specific heat effects

Figure 12 shows the calculated global heat release rates for the specific heat perturbation cases. For both test conditions, the specific heat perturbation had the largest impact on the calculated ignition delay, causing a -9.7 % ~ 9.1 % deviation from the baseline cases. The entire ignition process from the start of low temperature heat release to the transition to high temperature chemistry was slowest with the greatest specific heat.

To understand this behavior's root cause, reactivity contours for n-dodecane/air mixtures were calculated for each test condition just prior to heat release in the equivalence ratio – temperature domain as shown in Figure 13; markers noting the Φ and T in each cell are plotted onto the contours. For both cases, it is clear that the local temperatures decrease with increase in specific heat at a given equivalence ratio. This local temperature difference is caused by the change in the amount of thermal energy that should be transferred from the ambient charge to the liquid fuel for its vaporization (Q_{total} in Equation 4) as a result of liquid specific heat perturbation. With a higher specific heat, more thermal energy is required to increase the temperature of liquid fuel before its vaporization, which causes the lower local temperature. These local temperature

variations influence the local reactivity, where from the reactivity contour it is evident that the higher fuel specific heat case is colder and less reactive overall, resulting in a longer ignition delay.

Deviations in the ignition delay time caused by the specific heat perturbations, especially for the 750 K case, are ± ~0.2 ms, which is equivalent to ± ~2.4 crank angle degree at 2000 rpm. Such a change in ignition delay time or combustion phasing will have an effect on engine performance. Thus, emulating the specific heat of the liquid fuel should be considered for surrogates intended for spray/compression ignited combustion.

4.2 Density effects

Figure 14 shows the calculated global heat release rates for the density perturbation cases. Density affects the ignition delay time, showing up to a 7.1% deviation from the baseline case in Figure 11. An important observation is that high temperature ignition is retarded for the higher density 900 K case, while ignition is advanced with higher density in the 750 K one. Although the overall change in ignition delay time was not consistent, a common trend for each ignition event was slower LTHR progress and shorter NTC duration with greater liquid density.

One of the major reasons for these variations is the change in air/fuel mixing that results from the density variations. As discussed previously, when the injection pressure is kept constant (which was the case in this study), the density perturbation affects injection velocity (U_{fuel}), the mass injection rate ($\dot{m}_{fuel}$), and the resulting kinetic energy flow rate from the fuel injection ($\dot{E}_{kinetic,injection}$) as follows:

$$U_{fuel} \propto \sqrt{\frac{1}{\rho_{fuel}}} \qquad \text{(Eq. 5)}$$

$$\dot{m}_{fuel} \propto \sqrt{\rho_{fuel}} \qquad \text{(Eq. 6)}$$

$$\dot{E}_{kinetic,injection} \propto \dot{m}_{fuel}\left(U_{fuel}\right)^2 \propto \sqrt{\frac{1}{\rho_{fuel}}} \qquad \text{(Eq. 7)}$$

As indicated by Equation 7, the kinetic energy introduced by the fuel injection decreases as the fuel density increases, due to the reduction in U_{fuel}. Since fuel injection is the driving force for turbulent mixing within the initially quiescent spray chamber, the lower kinetic energy of the fuel injection event with higher density results in lower turbulent mixing rates. For the current CFD simulation setup with the RANS turbulence model, the turbulent diffusion of heat and mass are governed by the turbulent thermal diffusivity (K_t) and turbulent mass diffusivity (D_t) obtained from turbulent viscosity (μ_t) and turbulent Prandtl (Pr) and Schmidt (Sc) numbers:

$$K_t = K + c_p \frac{\mu_t}{\mathrm{Pr}_t} \quad \text{(Eq. 8)}$$

$$D_t = \frac{\mu_t}{\rho Sc_t} \quad \text{(Eq. 9)}$$

where K is the molecular thermal conductivity, c_p is the gaseous specific heat, Pr_t is the turbulent Prandtl number, and Sc_t is the turbulent Schmidt number. Figure 15 (a) compares the turbulent mass diffusivities of the density perturbations for the 900 K case at 0.25 ms and clearly shows that D_t is inversely proportional to the liquid fuel density. Since the turbulent component of thermal diffusivity is calculated in a similar manner to mass diffusivity, an identical trend was observed - higher liquid density results in lower thermal diffusivity and slower rates of heat transfer. Thus, the turbulent transport of heat and species should be slower for the higher fuel density case. In Figure 15(b), the turbulent thermal and mass transport rates of the baseline case are adjusted by changing the turbulent Prandtl (Pr_t) and Schmidt (Sc_t) numbers. As indicated by Equation 8 and 9, higher Pr and Sc numbers reduce the rate of turbulent thermal and mass transport. As shown in Figure 15 (a) and (b), these mixing and density perturbations have a similar effect on the turbulent mass diffusivities, indicating that the different effects have a similar impact on mixing rates.

The effect of density on turbulent mixing impacts the LTHR and NTC characteristics of the spray. To see the effect on LTHR progress, the temperature-equivalence ratio distributions are shown before the start of heat release in Figure 16 for the density perturbations. Unlike the

specific heat perturbations, which showed three distinct bands clustered in the T and Φ domain of Figure 13, there are no such deviations in the T - Φ distributions of the density perturbations, hence the bands overlap. Thus, the reactivity of the spray before LTHR cannot be compared solely based upon the T - Φ distribution. However, using the method shown in [39], the mass distributions in the local reactivity space can be used to distinguish their relative reactivity. Taking the local information of the sprays in Figure 16, the local reactivity of the density perturbation cases was calculated with the same method used for Figure 10. Figure 17 illustrates the mass distribution in the local reactivity space before the start of the LTHR. The 900 K case as shown in Figure 17 (a) indicates that the spray with higher liquid fuel density has a smaller mass in the most reactive regime, which instead has more mass within less reactive regimes. This trend is more obvious for the 750 K case in Figure 17 (b), where the mixing effect is more pronounced due to much longer ignition delay period. Thus, the slower turbulent mixing for the higher density case prepares the charge more slowly during ignition delay, creating a smaller mass of high reactivity mixture and the slower LTHR reaction rates in Figure 14.

Despite the slower LTHR progress, the NTC duration becomes shorter for the higher density case as shown in Figure 14. This behavior can be better understood through a numerical experiment where the turbulent thermal and mass diffusivities of the baseline case are perturbed during the NTC period to isolate the effect of mixing on the NTC duration. Figure 18 compares the global heat release rate and peak temperature evolution of the 750 K case when the turbulent thermal and mass transport coefficients are perturbed at the start of the NTC period, indicated by the "perturbation start" line in the figure. The ranges of the Pr_t and Sc_t perturbations reflect the change in turbulent thermal and mass diffusivity predicted for the density perturbation cases. While the heat release rate profile is virtually unchanged until 1.7 ms, it is evident that the local peak temperatures begin to diverge starting at 1.5 ms, with the slower mixing cases (higher Pr_t and Sc_t) achieving significantly higher peak temperatures and heat release rate at a given time. The T - Φ distributions during the NTC period (at 1.7 ms) are shown in Figure 19 (a), where the slower mixing case (Sc, Pr x 1.2) achieves a ~ 50 K higher peak temperature than the faster

mixing (Sc, Pr x 0.8) case. Since the cumulative heat release at 1.7 ms is very similar for both cases - see Figure 18 (a). The local temperature difference is caused by the change in the rate of turbulent transport, where the slower mixing case reduces mixing rates with the colder surroundings, which results in higher local temperature. Figure 19 (b) shows the mass distribution from Figure 19 (a) in temperature bins of 10 K. It is clear that the slower mixing case has more mixture mass within the highest temperature region. Such an effect leads to the earlier onset of high temperature chemistry and is the main reason for the shorter NTC durations with higher density, which is also confirmed by observing similar deviations in the NTC durations from the baseline case for the density and mixing perturbation cases (-0.2 ~ 1.5 ms for density perturbation, -0.17 ~ xx ms(currently running) for the mixing perturbation). Identical trend was observed when the turbulent mixing is perturbed during the NTC period for the 900K case (not shown).

As shown above, the liquid density perturbations have competing effects on LTHR progress and NTC duration – greater density makes LTHR phase longer but NTC duration shorter, which is caused by slower turbulent mixing rate. These effects are consistent for both of the 900 K and 750 K cases, as shown in Figure 20, which summarizes the deviations in LTHR peak timing (or the start of NTC) and NTC duration from the baseline case. Since the contribution of these two competing effects to the total ignition delay time changes drastically depending on the charge temperature, the fuel density effect on ignition delay reverses when transitioning from 900 K to 750 K. As seen in Figure 20, the contribution from the deviations in LTHR progress is greater than those during NTC for the 900 K case, while the change in NTC duration dominates the overall ignition delay change for the 750 K case. For this reason, the density effect on ignition delay was shown to be opposite in 900 K and 750 K.

5 Summary and Conclusions

CFD spray simulations were conducted to evaluate the effects of liquid fuel properties on liquid penetration and ignition delay during compression ignited combustion. The perturbation of the liquid physical properties was made to reflect the property ranges expected from hydrocarbon molecules that are frequently used in petroleum-derived transportation fuel surrogates. The following conclusions can be drawn from the current study:

1. Among the six physical properties considered in this study, density, viscosity, vapor pressure and specific heat have a significant impact on the liquid penetration length (4 % ~ 18 %). The effects of surface tension and heat of vaporization were minimal.
2. Under the simulated ambient conditions, ignition delay was very sensitive to perturbations in specific heat. A greater specific heat increases the energy required for fuel vaporization, resulting in lower mixture temperatures, a less reactive fuel spray and longer ignition delay.
3. Liquid density not only affects liquid penetration length but also has a significant effect on ignition delay time. Density variations have competing effects on LTHR and NTC duration. With higher density, LTHR progress is slower, but NTC duration is shorter. The main cause of this behavior is the change in turbulent thermal and mass transport rates due to the effects of liquid density on these parameters. Slower mixing rate in higher liquid density case was slower to form reactive mixture for LHTR, but during NTC period, it was beneficial for earlier onset of high temperature chemistry by achieving higher local temperature. Relative contribution of these competing effects to total ignition delay time changes drastically depending on ambient temperature, causing the importance of density to ignition delay to be different at different ambient temperatures.
4. Liquid fuel properties other than specific heat and density do not have significant impact on ignition delay time.

5. Surrogates for spray/diesel combustion should consider emulating liquid density, viscosity, volatility, and specific heat of targeted fuel to properly capture the liquid penetration and ignition delay characteristics of the target fuel.

Acknowledgements

Funding for this work was provided by the Automotive Research Center (ARC), A U.S. Army Center of Excellence in the modeling and simulation of ground vehicles at the University of Michigan, with funding from government contract DoD-DoA W56HZV-04-2-0001 through the U.S. Army Tank Automotive Research, Development, and Engineering Center.

The authors wish to thank Dr. Daniel Lee of Convergent Science for his technical assistance and for the provision of the CONVERGE CFD code used in this work. The authors also gratefully acknowledge the assistance of Dr. Peter Kelly Senecal of Convergent Science and Dr. Sibendu Som of Argonne National Laboratory for their technical assistance with the CFD simulations.

Disclaimer

Reference herein to any specific commercial company, product, process, or service by trade name, trademark, manufacturer, or otherwise, does not necessarily constitute or imply its endorsement, recommendation, or favoring by the United States Government or the Department of Army (DoA). The opinions of the authors expressed herein do not necessarily state or reflect those of the United States Government or the DoA, and shall not be used for advertising or product endorsement purposes.

References

[1] D. Kim, J. Martz, A. Violi, Combust. Flame 161 (2014) 1489–1498.
[2] S. Dooley, S.H. Won, M. Chaos, J. Heyne, Y. Ju, F.L. Dryer, K. Kumar, C.-J. Sung, H. Wang, M.A. Oehlschlaeger, R.J. Santoro, T.A. Litzinger, Combust. Flame 157 (2010) 2333–2339.
[3] S. Dooley, S.H. Won, J. Heyne, T.I. Farouk, Y. Ju, F.L. Dryer, K. Kumar, X. Hui, C.-J. Sung, H. Wang, M.A. Oehlschlaeger, V. Iyer, S. Iyer, T.A. Litzinger, R.J. Santoro, T. Malewicki, K. Brezinsky, Combust. Flame 159 (2012) 1444–1466.
[4] M.L. Huber, E.W. Lemmon, T.J. Bruno, Energy Fuels 24 (2010) 3565–3571.
[5] C.V. Naik, K.V. Puduppakkam, A. Modak, E. Meeks, Y.L. Wang, Q. Feng, T.T. Tsotsis, Combust. Flame 158 (2011) 434–445.
[6] G. Stiesch, Modeling Engine Spray and Combustion Processes, Springer, Berlin ; New York, 2003.
[7] J. Naber, D.L. Siebers, SAE 960034 (1996).
[8] D.L. Siebers, SAE 980809 (1998).
[9] D.L. Siebers, SAE 1999-01-0528 (1999).
[10] B.S. Higgins, C.J. Mueller, D.L. Siebers, SAE 1999-01-0519 (1999).
[11] C.L. Genzale, L.M. Pickett, S. Kook, SAE 2010-01-0610 (2010).
[12] S. Kook, L.M. Pickett, Fuel 93 (2012) 539–548.
[13] Z. Wu, Z. Zhu, Z. Huang, Fuel 85 (2006) 1458–1464.
[14] C. Arcoumanis, C. Bae, R. Crookes, E. Kinoshita, Fuel 87 (2008) 1014–1030.
[15] S.A. Basha, K.R. Gopal, S. Jebaraj, Renew. Sustain. Energy Rev. 13 (2009) 1628–1634.
[16] J. Yu, C. Bae, Proc. Inst. Mech. Eng. Part J. Automob. Eng. 217 (2003) 1135–1144.
[17] H.J. Kim, S.H. Park, C.S. Lee, Fuel Process. Technol. 91 (2010) 354–363.
[18] A.A. Salvi, D. Assanis, Z. Filipi, Energy Fuels 26 (2012) 4231–4241.
[19] S. Som, D.E. Longman, A.I. Ramírez, S.K. Aggarwal, Fuel 89 (2010) 4014–4024.
[20] Y. Pei, R. Shan, S. Som, T. Lu, D. Longman, M.J. Davis, SAE 2014-01-1117 (2014).
[21] Y. Ra, R.D. Reitz, J. McFarlane, C.S. Daw, SAE 2008-01-1379 (2008).
[22] K.J. Richards, P.K. Senecal, E. Pomraning, CONVERGE (Version 2.1.0), Convergent Science Inc., Middleton, WI, 2013.
[23] R.D. Reitz, R. Diwakar, SAE 870598 (1987).
[24] D.P. Schmidt, C.J. Rutland, J. Comput. Phys. 164 (2000) 62–80.
[25] S.L. Post, J. Abraham, Int. J. Multiph. Flow 28 (2002) 997–1019.
[26] A.B. Liu, D. Mather, R.D. Reitz, SAE 930072 (1993).
[27] A.A. Amsden, P.J. O'Rourke, T.D. Butler, KIVA-II: A Computer Program for Chemically Reactive Flows with Sprays, Los Alamos National Laboratory, 1989.
[28] P.K. Senecal, E. Pomraning, K.J. Richards, S. Som, ICEF2012-92043 (2012).
[29] P. Dagaut, M. Cathonnet, Prog. Energy Combust. Sci. 32 (2006) 48–92.
[30] W.J. Pitz, C.J. Mueller, Prog. Energy Combust. Sci. 37 (2011) 330–350.
[31] Design Institute for Physical Properties, Sponsored by AIChE, DIPPR Project 801 - Full Version, Design Institute for Physical Property Research/AIChE, 2012.
[32] K. Narayanaswamy, P. Pepiot, H. Pitsch, Combust. Flame 161 (2014) 866–884.

[33] Sandia National Laboratories, Engine Combust. Netw. (n.d.).
[34] L.M. Pickett, J. Manin, C.L. Genzale, D.L. Siebers, M.P.B. Musculus, C.A. Idicheria, SAE 2011-04-12 (2011).
[35] P.M. Lillo, L.M. Pickett, H. Persson, O. Andersson, S. Kook, SAE 2012-01-1239 (2012).
[36] P.M. Wilkinson, A. Van Schayk, J.P.M. Spronken, L..‑Van Dierendonck, Chem. Eng. Sci. 48 (1993) 1213–1226.
[37] C.E. Ejim, B.A. Fleck, A. Amirfazli, Fuel 86 (2007) 1534–1544.
[38] S. Som, S.K. Aggarwal, Combust. Flame 157 (2010) 1179–1193.
[39] J. Kodavasal, G.A. Lavoie, D.N. Assanis, J.B. Martz, Combust. Flame 162 (2015) 451–461.
[40] CHEMKIN 10112, Reaction Design, San Diego, 2011.

Tables

Table 1. Details of experimental spray data from Sandia National Laboratories [33–35] used for model validation

	Non-reacting		Reacting		
Ambient Temp.	900K	1100K	900K	1200K	750K
Ambient Density	22.8 kg/m^3	15.2 kg/m^3	22.8 kg/m^3	22.8 kg/m^3	22.8 kg/m^3
Ambient Pressure	~ 6 MPa	~ 5 MPa	~ 6 MPa	~ 8 MPa	~ 5 MPa
Ignition Delay[a]	-	-	0.398 ms	0.147 ms	1.723 ms
Ambient Composition (N_2/CO_2/H_2O/O_2,molar)	0.8971/0.0652/0.0377/0		0.7515/0.0622/0.0362/0.15		
Fuel	n-dodecane				
Fuel Temperature	373K				
Injector	Spray A (Serial # 210677), Common rail, Single hole, 90 μm diameter				
Injection Pressure	150 MPa				

[a] The average of three optically measured ignition delays in [35].

Table 2. Multipliers assigned to baseline properties for their perturbations.

	Perturb Min	Perturb Max
Density	0.92	1.2
Vapor Pressure	0.41	10
Viscosity	0.4	2
Surface Tension	0.7	1.25
Heat of Vaporization	0.8	1.16
Specific Heat Capacity	0.7	1.2

Figures

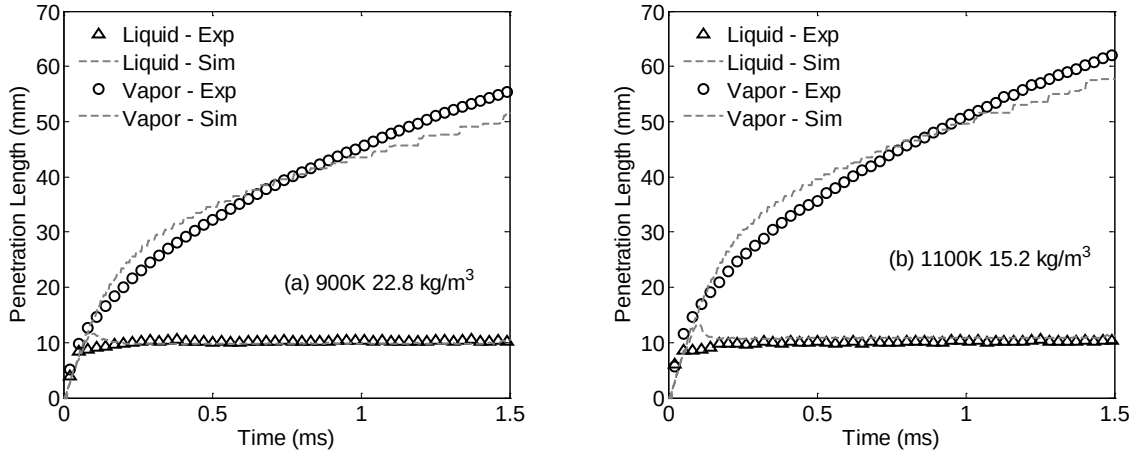

(a) (b)

Figure 1. Comparison of experimental liquid/vapor penetration measurements with the calculated liquid/vapor penetration lengths.

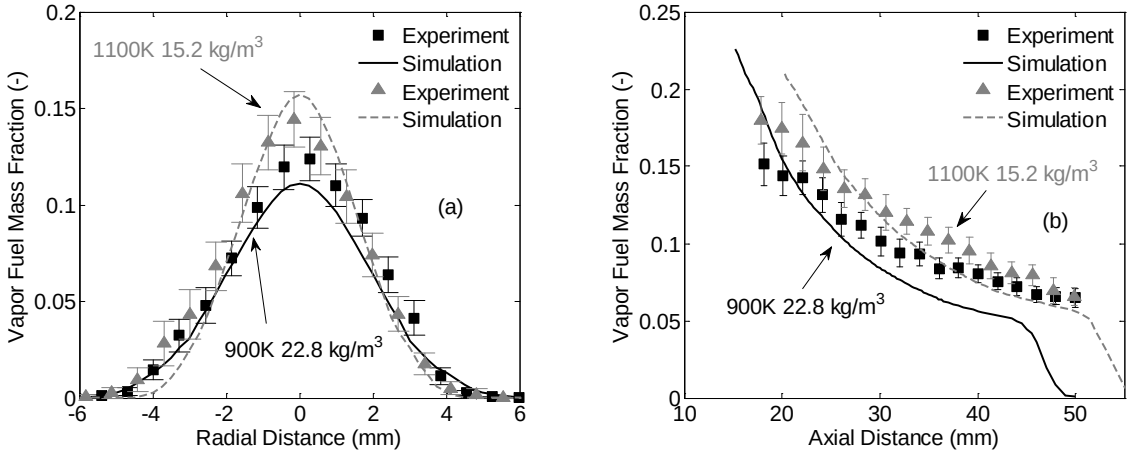

Figure 2. Comparison of experimental vapor fuel mass fraction [34] with the simulation results at (a) 25mm downstream from the injector tip and (b) centerline.

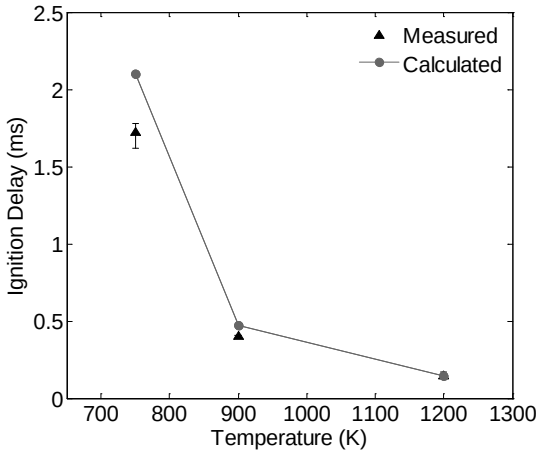

Figure 3. Comparison of measured and calculated ignition delays. Error bars show minimum and maximum values of three experiment runs.

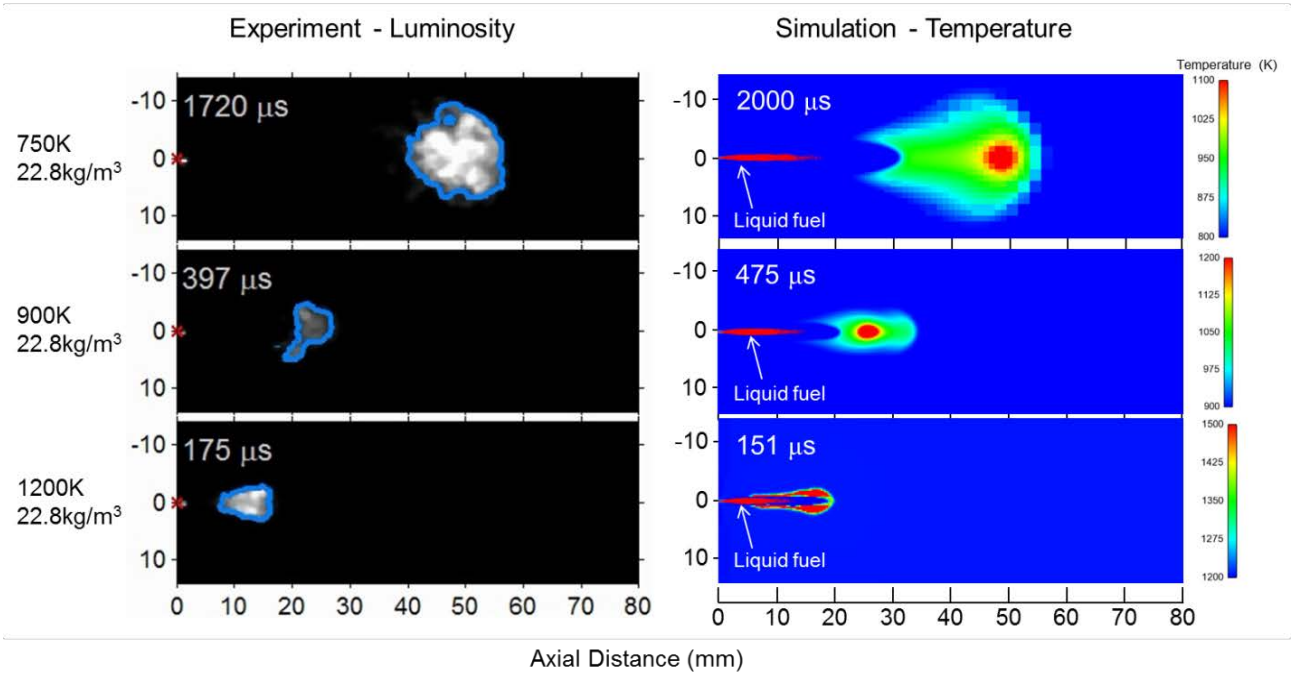

Figure 4. Comparison of chemiluminescence images from experiments [33] with predicted local temperatures near the time of ignition for reacting spray cases. For the luminosity images, regions inside blue borders are high temperature reactivity zones.

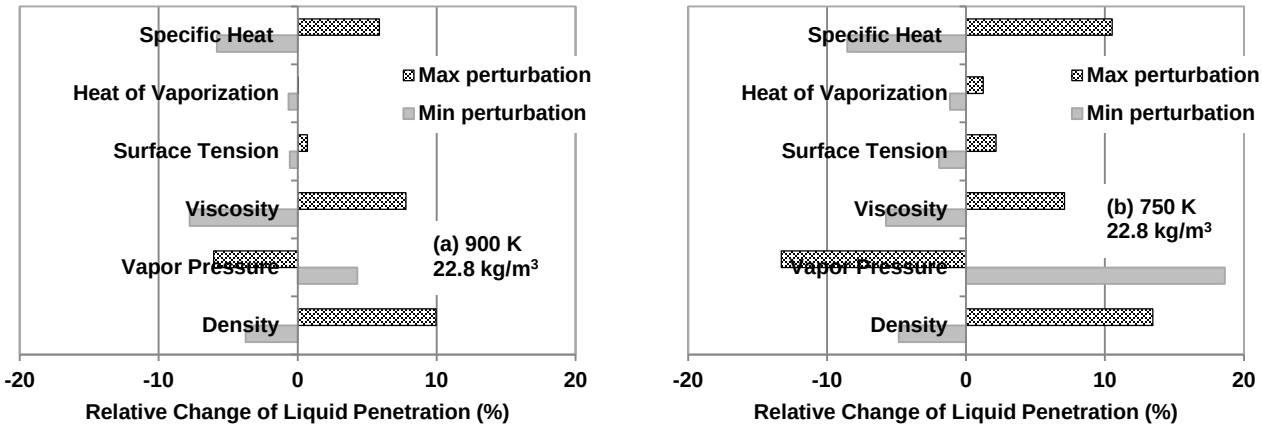

Figure 5. Relative change in liquid penetration length due to physical property perturbations at (a) 900 K 22.8 kg/m^3 and (b) 750 K 22.8 kg/m^3. The baseline liquid penetration length is 9.77 mm for (a) and 11.53 mm for (b).

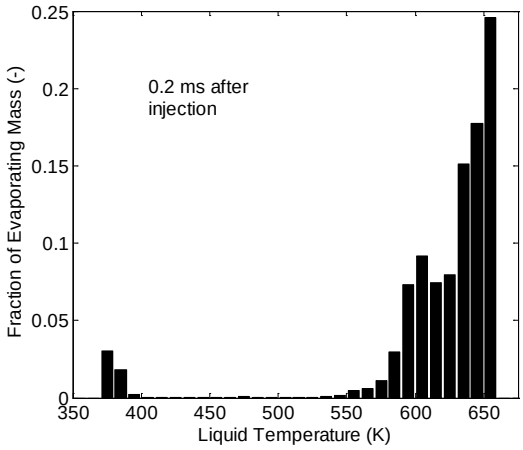

Figure 6. The evaporating mass fraction of each liquid droplet relative to the total evaporating mass at 0.2 ms after injection at 900 K 22.8 kg/m^3.

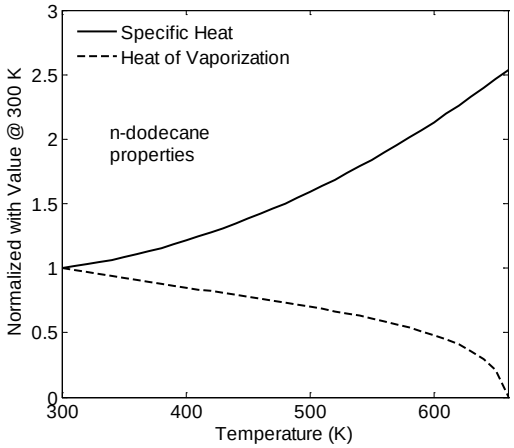

Figure 7. Temperature-dependent specific heat and heat of vaporization of liquid n-dodecane normalized to the value at 300 K

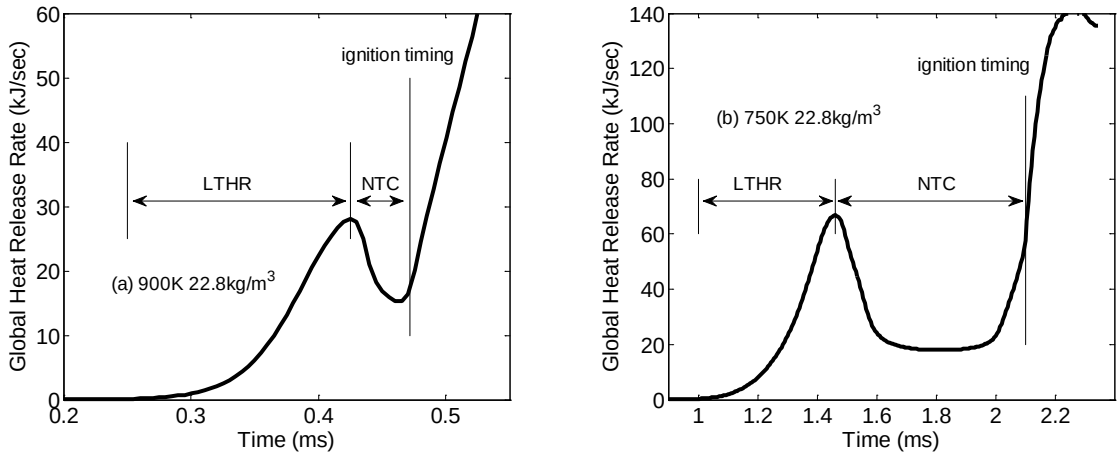

Figure 8. Calculated global heat release rates at (a) 900 K 22.8 kg/m^3 and (b) 750 K 22.8 kg/m^3 for the baseline cases. Marked ignition timing is defined as the time when the maximum rise rate of peak temperature occurs.

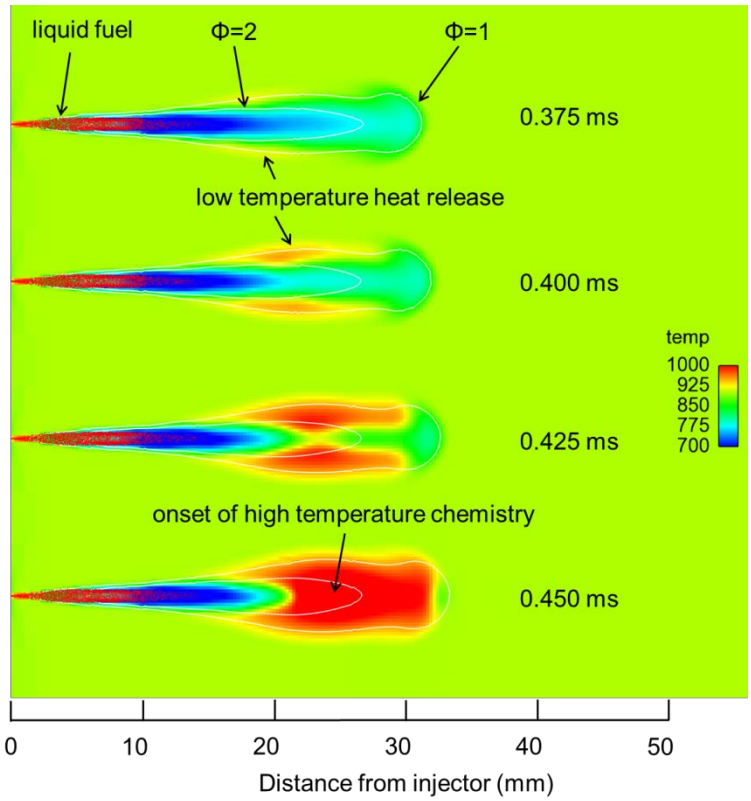

Figure 9. Calculated local temperatures at 900 K 22.8 kg/m^3 with the baseline fuel properties.

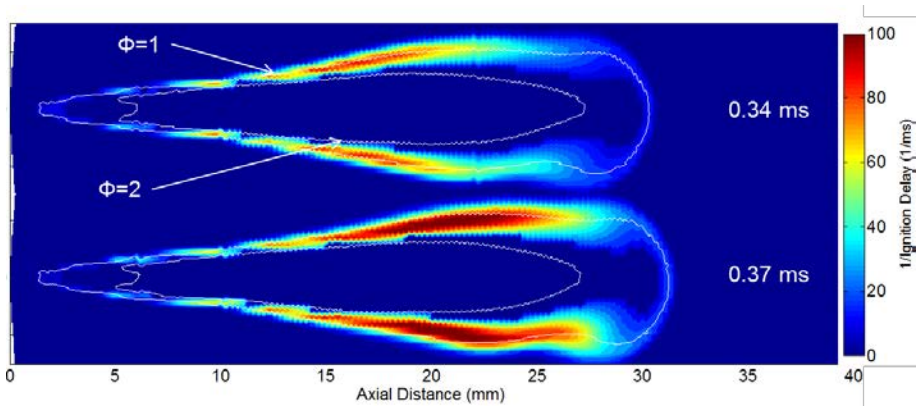

Figure 10. The local reactivity distribution during LTHR at 900 K 22.8 kg/m^3 with the baseline fuel properties.

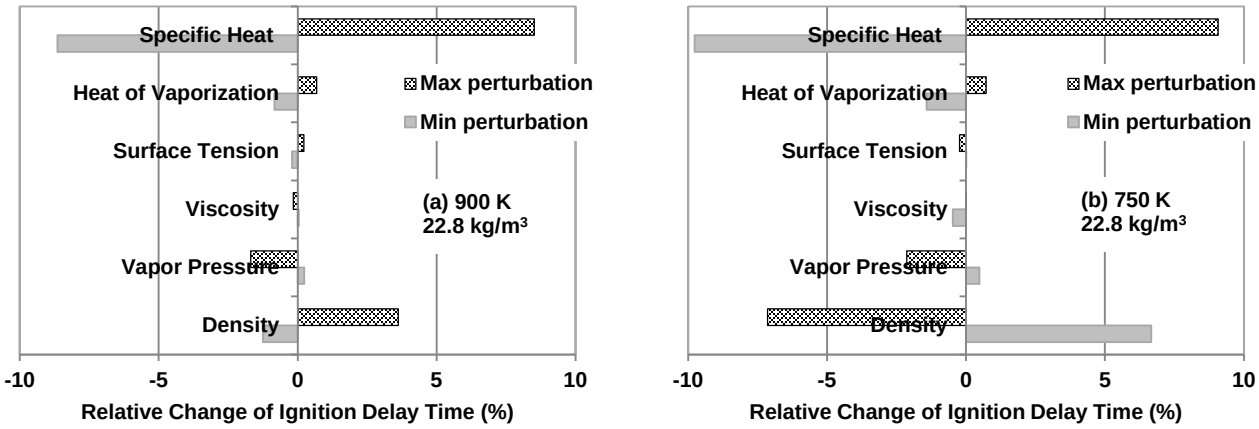

Figure 11. Relative change in ignition delay time due to physical property perturbation at (a) 900 K 22.8 kg/m^3 and (b) 750 K 22.8 kg/m^3. The baseline ignition delay is 0.472 ms for (a) and 2.100 ms for (b).

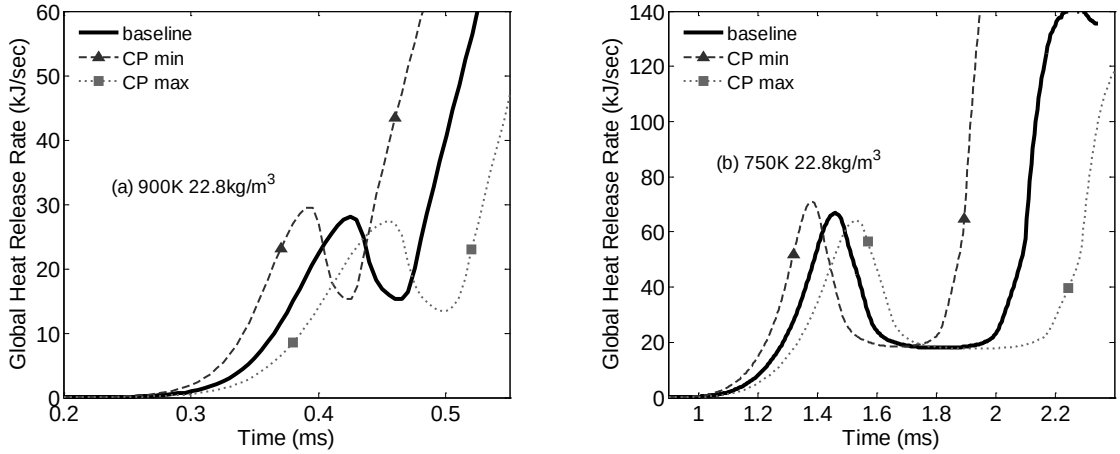

Figure 12. Comparisons of the calculated global heat release rates for the specific heat perturbation cases at (a) 900 K 22.8 kg/m^3 and (b) 750 K 22.8 kg/m^3.

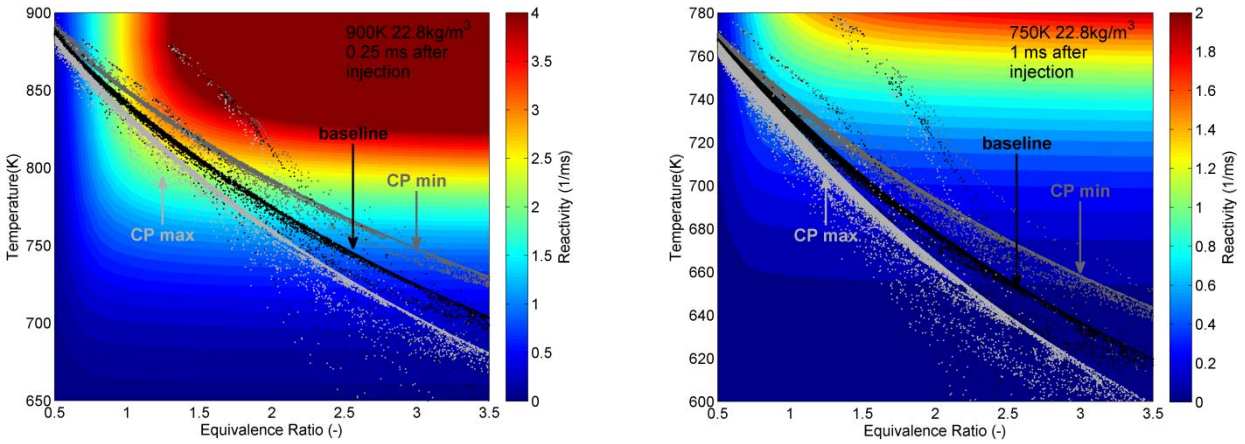

(a) (b)

Figure 13. The n-dodecane reactivity contour and temperature-equivalence ratio distribution within the spray before the start low temperature heat release for the specific heat perturbation cases. (a) 900 K 22.8 kg/m3 at 0.25 ms after injection with the reactivity contour at 60 atm and (b) 750 K 22.8 kg/m3 at 1 ms after injection with the reactivity contour at 50 atm.

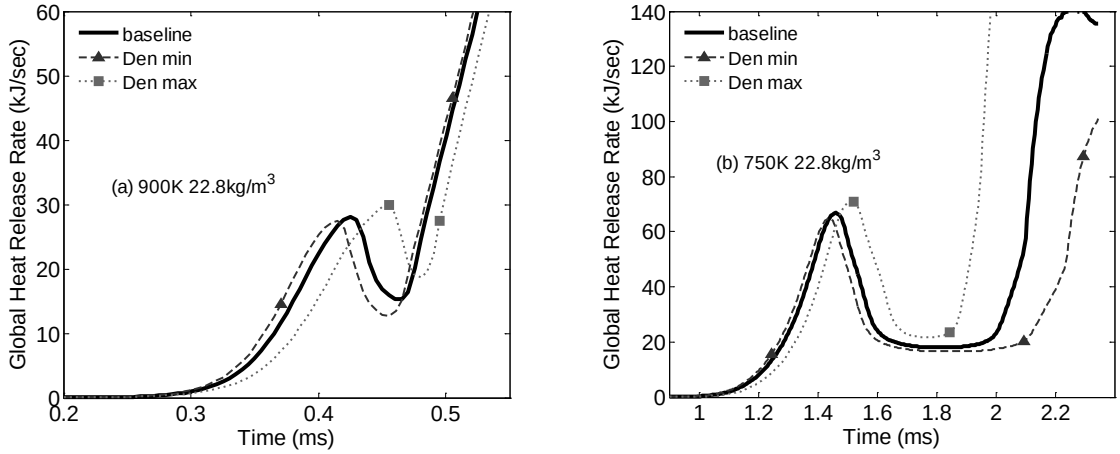

Figure 14. Comparisons of the calculated global heat release rates for the density perturbation cases at (a) 900 K 22.8 kg/m^3 and (b) 750 K 22.8 kg/m^3.

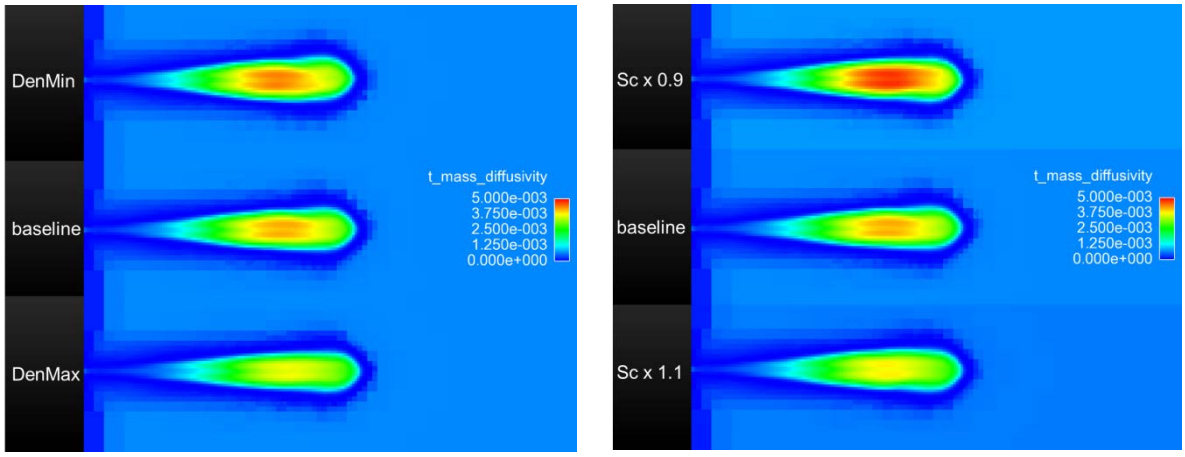

(a) (b)

Figure 15. Comparisons of turbulent mass diffusivity for 900 K 22.8 kg/m^3 case at 0.25ms after the start of the injection of (a) density perturbation cases and (b) mixing perturbation cases.

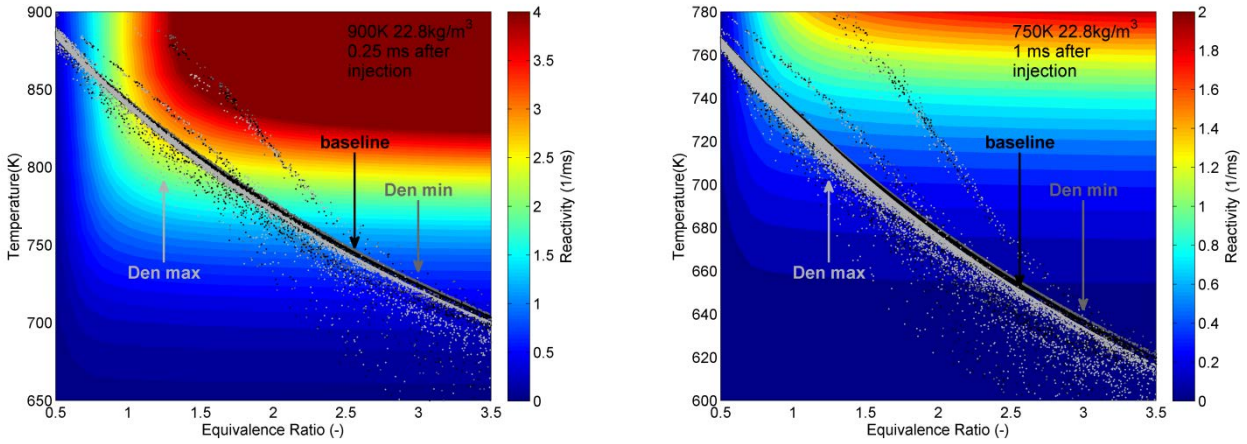

(a) (b)

Figure 16. The n-dodecane reactivity contour and temperature-equivalence ratio distribution within the spray before the start of low temperature heat release for the density perturbation cases. (a) 900 K 22.8 kg/m3 at 0.25 ms after injection with the reactivity contour at 60 atm and (b) 750 K 22.8 kg/m3 at 1 ms after injection with the reactivity contour at 50 atm.

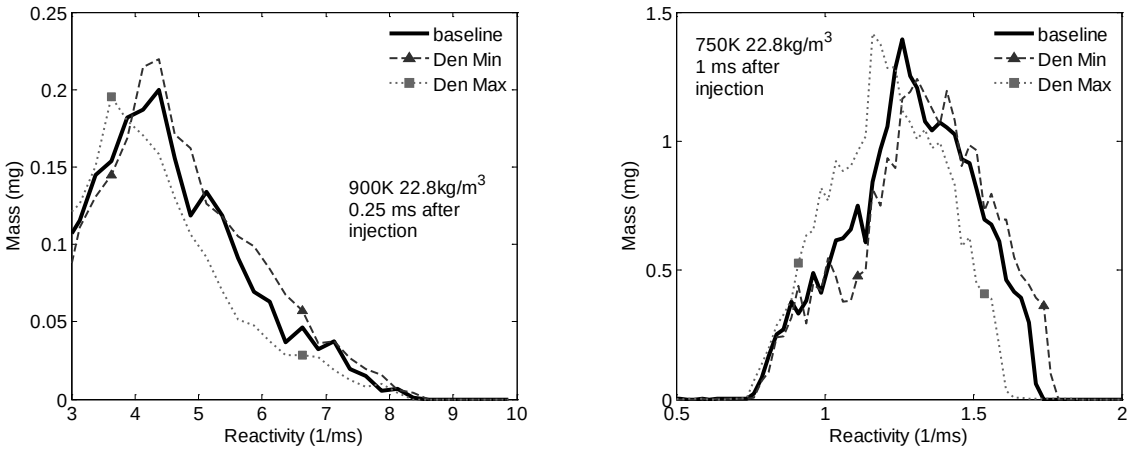

(a) (b)

Figure 17. Mixture mass distributions in the local reactivity domain before the start of low temperature heat release for the density perturbation cases for (a) 900 K 22.8 kg/m^3 at 0.25 ms after injection and (b) 750 K 22.8 kg/m^3 at 1 ms after injection. The reactivity bin size is 0.25 and 0.025 1/ms for the 900 K case and the 750 K case, respectively.

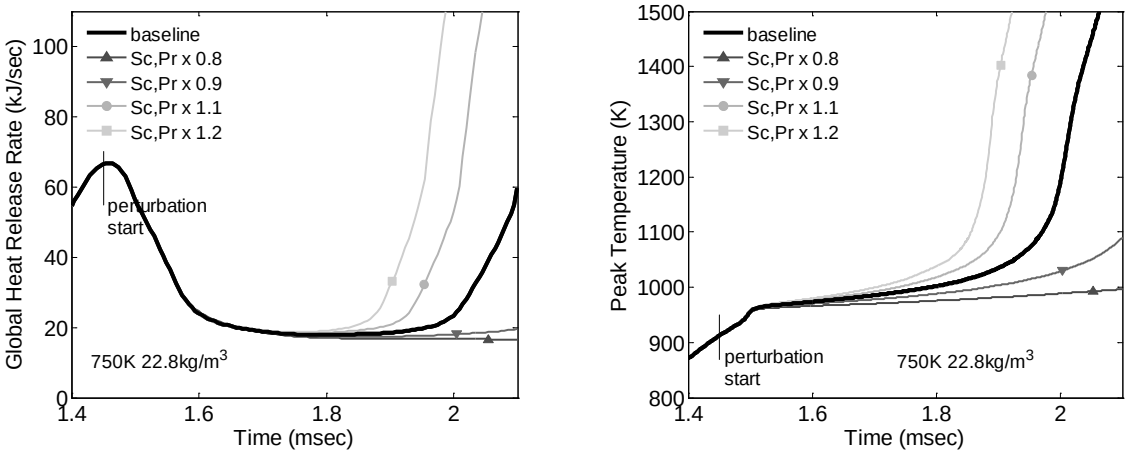

(a) (b)

Figure 18. (a) Global heat release rate and (b) peak temperature within the computation domain of mixing perturbation study during NTC period at 750 K 22.8 kg/m^3.

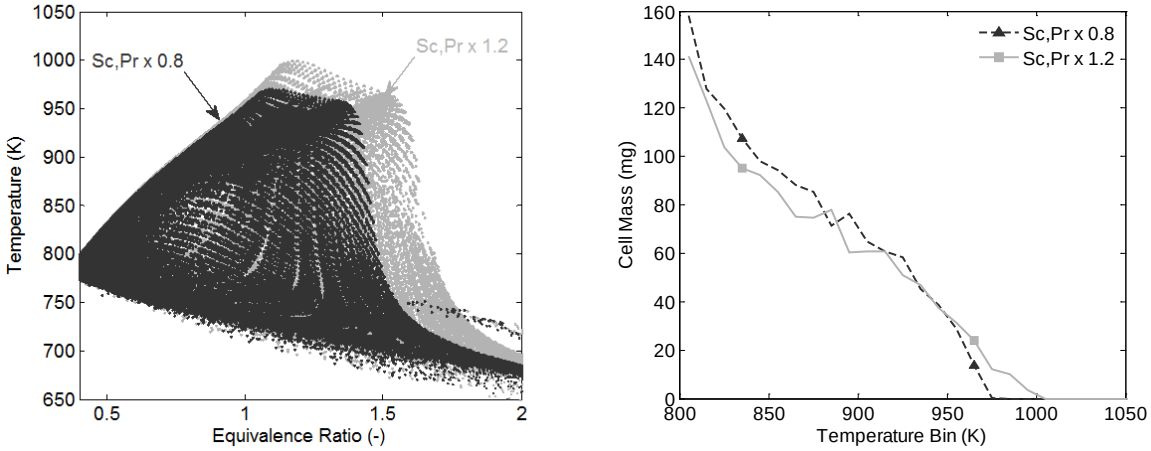

(a) (b)

Figure 19. (a) Temperature – equivalence ratio distributions and (b) mixture mass distribution in temperature domain (bins of 10 K) at 1.7 ms after start of injection for the mixing perturbation cases.

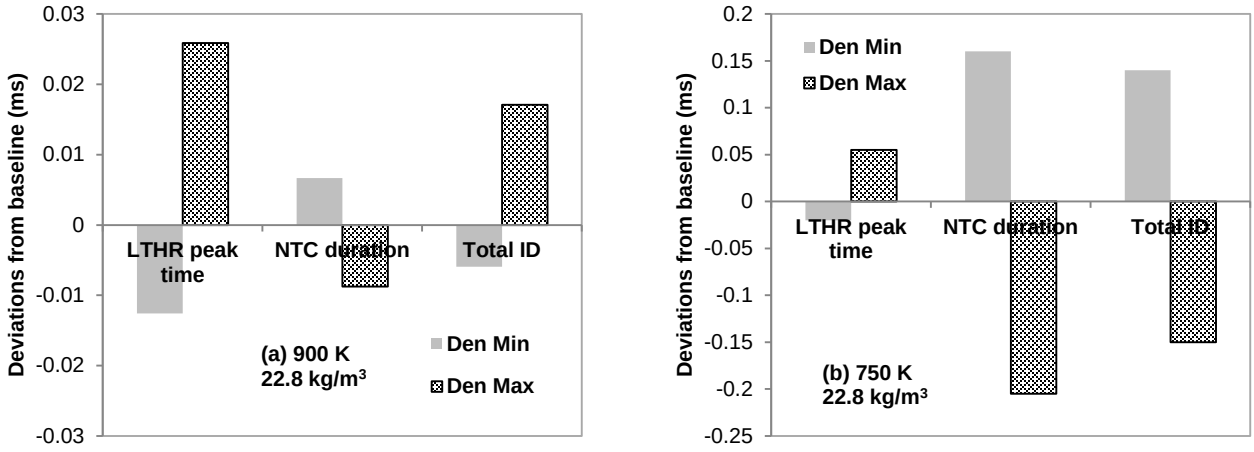

Figure 20. Deviations from the baseline in LTHR peak timing, NTC duration, and total ignition delay time for density perturbation cases at (a) 900 K 22.8 kg/m^3 and (b) 750 K 22.8 kg/m^3. The deviation in total ignition delay time is the sum of deviations in LTHR peak timing and NTC duration. The contribution from LTHR is greater for 900K, but dominated by the contribution from NTC duration for 750 K case.